

Miniature Single-Disk Viscous Pump (Single-DVP), Performance Characterization

Danny Blanchard

Phil Ligrani¹

e-mail: ligrani@mech.utah.edu

Bruce Gale

Department of Mechanical Engineering,
University of Utah,
50 South Central Campus Drive, Rm. 2110,
Salt Lake City, UT 84112

The development and testing of a rotating single-disk viscous pump are described. This pump consists of a 10.16 mm diameter spinning disk, and a pump chamber, which are separated by a small gap that forms the fluid passage. The walls of the pump chamber form a C-shaped channel with an inner radius of 1.19 mm, an outer radius of 2.38 mm, and a depth of 40, 73, 117, or 246 μm . Fluid inlet and outlet ports are located at the ends of the C-shaped channel. Experimental flow rate and pressure rise data are obtained for rotational speeds from 100 to 5000 rpm, fluid chamber heights from 40 to 246 μm , flow rates from 0 to 4.75 ml/min, pressure rises from 0 to 31.1 kPa, and fluid viscosities from 1 to 62 mPa s. An analytical expression for the net flow rate and pressure rise, as dependent on the fluid chamber geometry, disk rotational speed, and fluid viscosity, is derived and found to agree with the experimental data. The flow rate and pressure rise of the pump vary nearly linearly with rotational speed. The volumetric flow rate does not change significantly with changes in fluid viscosity for the same rotational speed and pumping circuit. Advantages of the disk pumps include simplicity, ease of manufacture, ability to produce continuous flow with a flow rate that does not vary significantly in time, and ability to pump biological samples without significant alteration or destruction of cells, protein suspension, or other delicate matter. [DOI: 10.1115/1.2175167]

Introduction

There is a need to circulate or move fluid through macroscale and/or microscale channels in many applications, including micro-sensors, separation devices, drug delivery systems, electronics cooling, and other small-scale and microscale fluidic devices. Many different micropumps are proposed to meet this need, generally to fulfill specific applications [1]. These include membrane pumps [2–8] (both without check valves [2–5] and with check valves [6–8]), electrohydrodynamic pumps [9–11], electrokinetic pumps [12,13], viscous pumps [14,15], rotary pumps [16,17], peristaltic pumps [4,18–20], ultrasonic pumps [21,22], and several other types of pumps [23–26]. Many of these micropumps are fabricated using microfabrication technology. Nonmechanical pumps like the electrohydrodynamic and electrokinetic pumps do not have moving parts, which increases reliability. However, such devices are generally limited by low flow rate and pressure rise capabilities, the applications of the pump, the working fluids that can be pumped, and high supply voltage requirements [1]. Mechanical pumps like rotary pumps, peristaltic pumps, and membrane pumps have a wide variety of possible working fluids and applications. However, such mechanical micropumps are believed to be feasible only when they are greater than a certain size [1], due to the large viscous forces in the fluid at small pump geometries. At very small scales, the viscous forces are significant, and result in large pressure drops over small lengths for fluid flow through a channel [27]. One motivation of the present effort is to employ these large viscous forces to produce a millimeter-scale pump with an easily adjusted, constant flow rate.

Many variations of macroscale viscous pumps have been proposed [28–34]. Most of these pumps have a linear relationship between flow rate and pressure rise for a range of operating parameters and pump geometries. Viscous pumps are ideal for applications where high pressure rises, and low to moderate flow

rates are required [34]. Uses of different viscous pumps at micro-scales are described by Sen et al. [15], and Kilani et al. [14]. Sen et al. [15] presents a pump that employs a shaft whose axis is perpendicular to the flow direction, and is positioned eccentrically in a channel. The difference in viscous shear between the shaft and the two channel walls produces a net pumping effect. Numerical simulations are performed by Sharatchandra et al. [35] to determine the optimal configuration. This pump is easy to fabricate, but has limited flow rates and pressure rise capabilities. Kilani et al. [14] describes a spiral pump that uses one spinning disk rotating over a single spiral channel to produce a pumping effect. Results from a macroscale version of this pump are consistent with an analytical expression for flow rate and pressure rise [14]. A small-scale version of this pump may be complex to fabricate.

A new viscous micropump is presented, called the single-disk viscous pump (single-DVP), to achieve easily controlled flow rates and pressure rises while maintaining simplicity and ease of manufacturing. An analytical equation is presented, based on the Navier-Stokes equations, which relates pressure rise and flow rate to the pump geometry, rotational speed and working fluid properties. The predicted performance of the pump from the analytical equation is compared to experimental data. The disk pump is unique because it uses viscous stress to produce a pumping effect by employing one disk and a C-shaped channel [36]. Figure 1 shows external and internal views of the single-DVP. The spinning of the disk causes a net movement of fluid due to the viscous stresses imposed on the fluid from the spinning disk. As the fluid passage height becomes smaller, the Reynolds number decreases, and the viscous forces become more significant than inertial forces. Thus, one assumption employed in the flow analysis is that the inertial or advection terms in the Navier-Stokes equations are insignificant compared to the diffusion of momentum terms. Following this analysis, the development, fabrication, and testing of the disk pump is discussed. The flow rate and pressure rise for various rotational speeds are measured experimentally and compared to analytical expressions for the flow rate and pressure rise. Based on such results, advantages of this micropump compared to other micropumps are identified and discussed, and include a wide range of possible flow rates, simplicity, planar structure, well con-

¹Corresponding author.

Contributed by the Fluids Engineering Division of ASME for publication in the JOURNAL OF FLUIDS ENGINEERING. Manuscript received April 21, 2005; final manuscript received September 29, 2005. Review conducted by Joseph Katz.

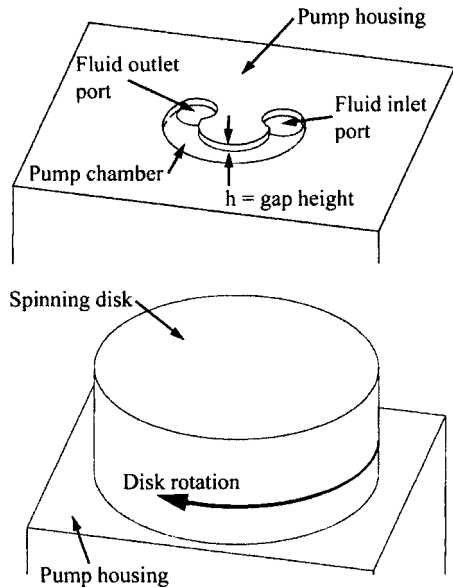


Fig. 1 External and internal views of the single-disk viscous pump

trolled flow rate, ease of manufacture, and ability to produce continuous flow with a flow rate that does not vary significantly in time. The device also has the ability to pump biological samples without significant alteration or destruction of cells, protein suspension, or other delicate matter. This is because shear levels produced by the present device for the present range of experimental conditions are always less than 10^5 1/s, which is the shear value when red blood cells (erythrocytes) as well as types of other biological samples begin to be damaged. With this in mind, micro-scale applications that may be suitable for a viscous pump include pumping of biomedical fluids, drug delivery devices, μ -TAS, fluidic sensors, and mixing devices.

Single-Disk Viscous Pump Configuration and Operation

The single-disk viscous pump (single-DVP) is comprised of a spinning disk, and a C-shaped channel that forms the pump chamber with a fluid inlet port and a fluid outlet ports located at opposite ends. Figure 1 shows an external view and an internal cross-sectional view of the single-DVP. The disk contacts the fluid chamber walls to create a seal to minimize leakage from the pump chamber. The height of the pump chamber is the distance between the disk surface and the top of the pumping chamber, and is referred to as the flow passage height of the pump. The flow passage heights used for testing in this work are 40, 73, 117, and 246 μ m. As the disk spins, a rotating Couette-type flow is induced in the fluid chamber between the disk and the stationary top surface of the fluid chamber.

A circumferential pressure gradient is present in the fluid chamber mostly because of interactions between the fluid and the walls at the ends of the C-shaped channel. This interaction gives a static pressure rise with circumferential position through the pump chamber volume, such that a region of lower static pressure is present near the fluid inlet port, and a region of higher static pressure is present near the fluid outlet port. This static pressure variation then opposes the motion induced by the disk rotation and viscous forces. If the opposing circumferential static pressure variation is large enough, some of the fluid between the spinning disk and top surface of the fluid chamber will recirculate in the opposite direction of the disk rotation. For the case when the fluid outlet port is closed (or a valve on the outlet tubing is closed), there is fluid movement in the pump chamber, but the net flow rate

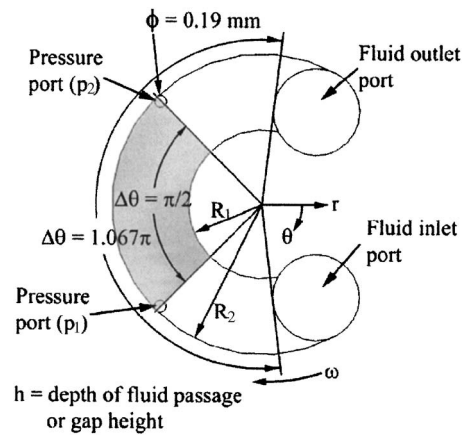


Fig. 2 Configuration of the single-disk viscous pump. The shaded region of the pump chamber is used for the flow analysis.

of the fluid velocity over a cross section of the disk pump flow passage is zero. The resulting pressure rise is referred to as the maximum pressure rise.

Flow Analysis for the Single-Disk Viscous Pump

Derivation of an expression for pressure rise and flow rate in terms of pump geometry, disk rotational speed, and fluid properties is required to properly design, develop, and analyze a functional viscous disk pump. The analysis that follows leads to an expression for pressure rise and flow rate as dependent upon pump geometry, disk rotational speed, and fluid properties. Figure 2 shows a cross-sectional view of the single-DVP flow passage. The shaded region in this figure is used for the flow analysis.

In this flow analysis, an incompressible, steady flow of a Newtonian fluid, with constant density and viscosity is considered. Assuming that $h \ll (R_2 - R_1)$, edge effects near the inner radius and outer radius can be ignored. Also assume that gravity is negligible, and the rotational speed of the disks is slow enough such that the body force due to centrifugal acceleration is negligible compared to the forces produced by gradients of viscous stresses, and gradients of pressure. This assumption is valid for low Reynolds number flows. The gradients of viscous stresses are assumed to be more significant than the inertial or advection terms in the Navier-Stokes equation because the fluid motion is produced by viscous forces, and because the flow passage height is small. The Navier-Stokes equation with neglected inertial or advection terms, in cylindrical coordinates, is given by [37]

$$\frac{1}{r} \frac{\partial p}{\partial \theta} = \mu \left[\frac{\partial}{\partial r} \left(\frac{1}{r} \frac{\partial}{\partial r} (rv_\theta) \right) + \frac{1}{r^2} \frac{\partial^2 v_\theta}{\partial \theta^2} + \frac{\partial^2 v_\theta}{\partial z^2} + \frac{2}{r^2} \frac{\partial v_r}{\partial \theta} \right] \quad (1)$$

Equation (1) shows that the circumferential pressure gradient (left side) is equal to the diffusion of circumferential momentum terms (right side). Thus, the pressure gradient changes as the viscous stress imposed on the fluid by the spinning disk change. Increasing the viscous stresses then also increases the pressure gradient, for example, increasing the fluid viscosity or by increasing the disk rotational speed.

For this analysis, flow in the pumping region indicates by the shaded area in Fig. 2 is considered. For a cylindrical coordinate system, the velocity $v_\theta \gg v_z$, so that the z component of velocity at all locations can be approximated as $v_z = 0$. In addition, if it is assumed that $h \ll 3R_1 \pi/2$ (circumference of the inner radius of the pump chamber), the flow in this region can be approximated as fully developed in the θ direction. Assuming incompressible, steady, fully developed flow, and the continuity equation becomes

$$\frac{1}{r} \frac{\partial}{\partial r}(rv_r) = 0 \quad (2)$$

From this equation, the value of rv_r is equal to a constant. At $r = R_1$ (inner radius wall), $v_r = 0$, which implies that $v_r = 0$ in the entire region being considered. The pressure gradients for the z and r directions are then given by

$$\frac{\partial p}{\partial z} = 0 \quad (3)$$

and

$$\frac{\partial p}{\partial r} = 0 \quad (4)$$

respectively. Equations (3) and (4) show that the pressure gradient is invariant in the z and r directions.

When the gap is thin, that is $h/(R_2 - R_1) \ll 1$, changes of v_θ across the z direction over the distance h are much larger than the changes of v_θ in the r direction over the distance $R_2 - R_1$. Therefore the first term on the right side of Eq. (1) is ignored. The second term on the right side of Eq. (1) is ignored because of the fully developed flow assumption made previously. The fourth term on the right side of Eq. (1) is ignored because $v_r = 0$. The resulting equation is then simplified as follows

$$\frac{1}{r} \frac{\partial p}{\partial \theta} = \mu \frac{\partial^2 v_\theta}{\partial z^2} \quad (5)$$

The circumferential velocity (v_θ) does not change with circumferential position, with the fully developed flow and incompressible fluid assumptions mentioned previously. Thus, because mass must be conserved, the pressure gradient on the left-hand side of Eq. (5) must be constant in the θ direction, which results in a linear pressure rise in the θ direction. The pressure gradient in the θ direction is then approximated using

$$\frac{\partial p}{\partial \theta} \approx \frac{\Delta P}{\Delta \theta} \quad (6)$$

where ΔP is the pressure rise over the angle $\Delta \theta$. The pressure rise between the two pressure ports ($p_2 - p_1$) shown in Fig. 2 is denoted as ΔP_{2-1} , and the pressure rise between the fluid inlet and outlet ports shown in Fig. 2 is denoted as ΔP_{out-in} . In addition $\Delta \theta$ is the angle between the pressure ports ($\Delta \theta = \pi/2$) or between the inlet and outlet ports ($\Delta \theta = 1.067\pi$), as shown in Fig. 2.

The velocity profile $v_\theta(r, z)$ is determined by solving the ordinary differential equation given by Eq. (5), with the following boundary conditions for the single-DVP

$$v_\theta(r, h) = 0 \quad (7)$$

$$v_\theta(r, 0) = r\omega \quad (8)$$

The resulting velocity profile is given by

$$v_\theta(r, z) = \frac{h^2}{2\mu r} \frac{\Delta P}{\Delta \theta} \left[\left(\frac{z}{h} \right)^2 - \frac{z}{h} \right] + \frac{r\omega}{h} z \quad (9)$$

The volumetric flow rate is determined by integrating the velocity profile over a radial cross section of the pump chamber, from $z = 0$ to $z = h$, and from $r = R_2$ to $r = R_1$ as given by

$$Q = \int_0^h \int_{R_1}^{R_2} v_\theta(r, z) dr dz = \frac{h^3 \ln(R_1/R_2)}{12\mu} \frac{\Delta P}{\Delta \theta} + \frac{\omega h(R_2^2 - R_1^2)}{4} \quad (10)$$

Equation (10) describes the flow of the single-DVP as dependent upon pressure rise (ΔP), pump geometry (R_1 , R_2 , $\Delta \theta$, and h), disk angular velocity (ω), and fluid viscosity (μ).

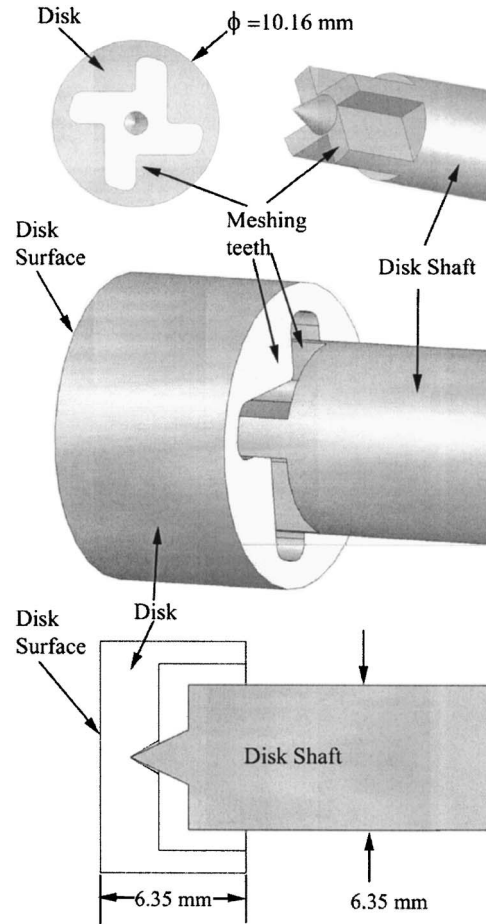


Fig. 3 Cross-sectional view and assembled view of the disk and disk shaft

Pump Component Fabrication

There are three main fabricated components of the rotary shaft pump assembly: (i) the disk, (ii) the disk shaft, and (iii) pump chamber contained within the pump housing.

The disk surface must be flat so that it is aligned with the top surface of the pump chamber, because any misalignment of the disk will result in leakage and flow passage height variation across the pump chamber. The disk surface is aligned when the disk surface is flush against the bottom of the pump housing. The disk is therefore designed to be self-aligning to ensure that the disk surface is flush against the bottom surface of the pump housing, and thus, parallel to the top of the fluid chamber (since the fluid chamber is uniform in depth). Figure 3 shows the back of the disk, the disk shaft and a cross-sectional view and assembled view of the disk and disk shaft together, all of which are designed to meet these requirements. The disk is constructed with a 60 deg cone indentation and is driven by meshing teeth on the disk shaft. The point on the cone of the disk shaft transmits a single-point axial force that holds the disk in position, while also providing a pivot point so that the disk surface can align to the bottom surface of the pump housing. Figure 3 also shows arrangements of the meshing teeth of the disk and disk shaft. The meshing teeth transmit the torque required to rotate the disk, while still allowing some movement required to keep the disk flat and aligned relative to the bottom surface of the pump housing.

Precision machining techniques are used to fabricate the disk and disk shaft. A lathe is used to obtain the desired outside diameter of the disk, and to create the disk surface. The disk is made from PEEK plastic (Ensinger Engineering Plastics, Washington

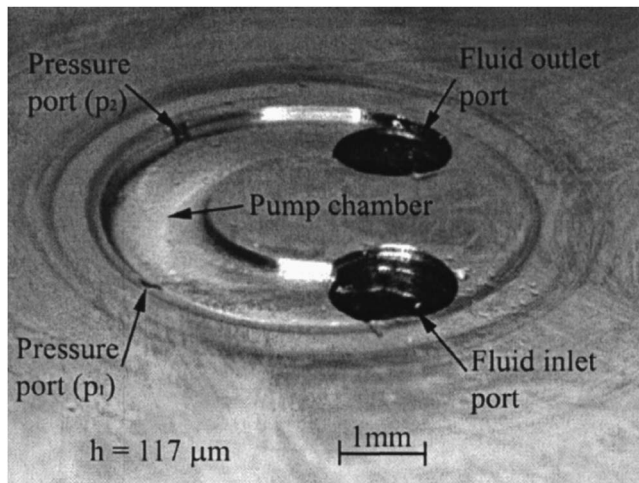


Fig. 4 Image of the single-disk viscous pump housing containing the pump chamber. The pump chamber depth or flow passage height is $117\ \mu\text{m}$, with a pump chamber outer radius of $2.38\ \text{mm}$.

PA) with a final outer diameter of $10.16\ \text{mm}$. The cone on the disk is made using a $60\ \text{deg}$ scribe tool. The disk surface is polished to produce a smooth flat surface. The meshing teeth of the disk and disk shaft are machined with a CNC milling machine. The cone shape on the disk shaft is made using a lathe. The disk shaft is made using type 17-4 stainless steel.

The C-shaped channel that defines the pump chamber is machined into the pump housing. The inner and outer radii of the C-shaped channel are 1.19 and $2.38\ \text{mm}$, respectively. The pump housing is made using type 17-4 stainless steel block that is $19\ \text{mm}$ thick. The fluid chamber is cut into the bottom face of the pump housing using a CNC milling machine. The face of the steel block is polished to produce a smooth flat surface. The final flow passage height of the fluid channel is measured with a Tencor P-10 profilometer, with a $327\ \mu\text{m}$ vertical range and a resolution of $0.195\ \text{\AA}$. The flow passage height variation across the fluid chamber, including roughness and flatness, is then less than $1.5\ \mu\text{m}$. Holes for the pressure ports are drilled with a $0.19\ \text{mm}$ diameter drill bit. Holes for the fluid inlet and outlet ports are $1.397\ \text{mm}$ in diameter. A photograph of the machined fluid chamber with fluid inlet and outlet ports, and pressure ports is shown in Fig. 4. Four holes are drilled from the top of the pump housing, and connect to the pressure ports and fluid inlet and outlet ports. Tubing is press fit into these four holes on the top of the pump housing to interface the fluid chamber with fluid reservoirs, and a differential pressure transducer.

Experimental Apparatus and Procedures

The disk pumps are powered by an externally mounted Maxon EC32 number 118891, brushless DC motor that is $32\ \text{mm}$ in diameter, with an $80\ \text{W}$ power rating. The maximum speed is $25,000\ \text{rpm}$, with a stall torque of $0.35\ \text{N}\cdot\text{m}$. The brushless motor is controlled by an Advanced Motion Controls power amplifier (Model #BE12A6). The power amplifier has a DC supply voltage of $40\ \text{V}$, a peak current of $12\ \text{A}$, and continuous current rating of $6\ \text{A}$. A negative feedback controller is employed to maintain constant speed for any variation in torque. The speed is controlled by adjusting a 15-turn potentiometer. The rotational speed range used for testing is $100\text{--}5,000\ \text{rpm}$. The motor controller determines the rotational speed from the signal from an optical encoder attached to the motor shaft. This apparatus produces a voltage signal that is proportional to speed. The voltage is measured using a National Instruments PCI-6013 data acquisition card and LABVIEW 7.0 software.

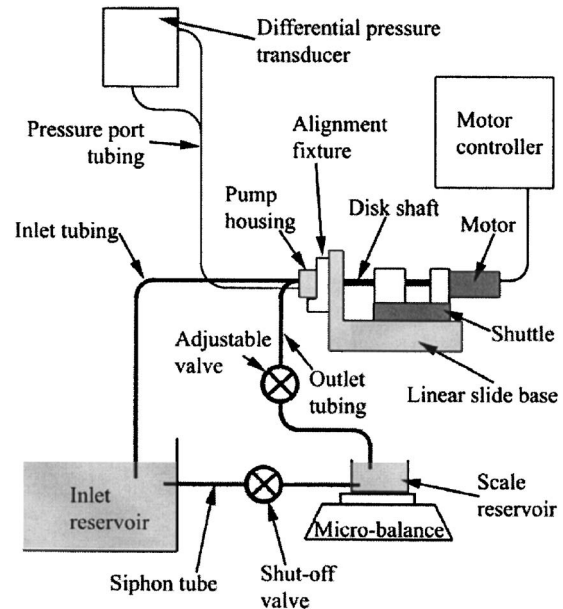


Fig. 5 Test setup for the single-disk viscous pump

The test setup is shown in Fig. 5 and includes an inlet reservoir and scale reservoir, which are large enough that the water level change during operation is negligible. The inlet reservoir is connected to the fluid inlet port by means of inlet tubing, with an inner diameter of $4.5\ \text{mm}$ and a length of $508\ \text{mm}$. The inlet tubing steps down to an outer diameter of $1.59\ \text{mm}$, with an inner diameter of $1.397\ \text{mm}$, that is press-fit into the top of the pump housing. The fluid outlet port is connected to the outlet tubing, which starts with inner and outer diameters of 1.397 and $1.59\ \text{mm}$, respectively, that is press-fit into the top of the pump housing, and then steps up to an inner diameter of $4.5\ \text{mm}$. An adjustable valve is incorporated into the outlet tubing for adjustment of the flow rate through the fluid chamber. The outlet tubing drains to the scale reservoir on a Mettler AE-163 microbalance with accuracy to $0.1\ \text{mg}$. A siphon tube connects the water reservoir on the balance to the inlet water reservoir. A shut-off valve is incorporated into the siphon tube to allow or stop fluid flow through the siphon tube.

A DP-15 Validyne differential pressure transducer is used to measure the differential pressure between the pressure ports. Two different diaphragms are used to accommodate different ranges of pressure differentials, with maximum gauge pressures of $872\ \text{Pa}$ and $13.8\ \text{kPa}$. The output signal from the pressure sensor is processed using a Celesco Model number CD10D Carrier Demodulator, which produces a voltage output that is proportional to pressure. The voltage is read by the data acquisition board and LABVIEW 7.0, mentioned previously.

The pump assembly is mounted to the base of a linear slide. The brushless motor and disk shaft are mounted to the shuttle of the linear slide as shown in Fig. 5. The disk shaft is supported with two bearings, and the distal end of the disk shaft connects to the motor shaft. Elastic bands are employed to exert a constant force on the shuttle in the direction of the pump chamber to keep the disk surface flush against the bottom of the pump housing. An alignment fixture is used to mount the pump housing and pump chamber, such that the axis of the disk aligns with the center point of the pump chamber radius. The working fluids employed are water, and 5W-30 motor oil, with properties given in Table 1. Note that 5W-30 motor oil is slightly non-Newtonian for shear rates greater than about $2500\ \text{s}^{-1}$. Just after assembling the disk, disk shaft, and pump chamber, and just prior to testing, the fluid inlet and outlet tubing and pressure port tubing are press-fit into

Table 1 Fluid properties of water, and oil used for experimental testing

Working fluid	ρ (kg/m ³)	μ (at 30°C) (Pas)
Water	1000	0.0010
5W-30 motor oil	857	0.0630

the top of the pump housing. The air is then bled from the pump chamber assembly using syringes filled with working fluid that are attached to the end of the inlet tubing and pressure transducer. The syringes are removed after the air is bled from the system.

After these steps are completed, testing is comprised of the following procedures. (1) The system is flushed to ensure there are no air bubbles or trapped particulates in the pump chamber. (2) The shut-off valve on the siphon tube is opened until the surface level of the inlet fluid reservoir and scale reservoir are equal. (3) The shut-off valve on the siphon tube is closed. (4) The adjustable valve on the outlet tubing is adjusted to achieve the desired flow rate. (5) The motor is activated, and adjusted to produce the desired speed. (6) The motor then continues to operate at constant speed until steady state is reached. Steady state is reached when the average pressure rise measurement is constant. (7) For testing with a net volumetric flow rate, the time is started and the scale display is recorded every minute for 3 min. Output signals related to shaft rotational speed, and pressure rise ΔP_{2-1} are recorded every minute for 3 min using the NI data acquisition card and LABVIEW 7.0 discussed previously. The flow rate is determined by dividing the amount of water collected (mass change multiplied by the fluid density) by the collection time. All data are recorded, entered, and processed using a computer.

Uncertainty Analysis

A first-order uncertainty analysis is performed using a constant-odds combination method, based on a 95% confidence level as described by Moffat [38]. The variation of flow passage height across the fluid chamber contributes most to the uncertainties associated with measurement of pressure rise and flow rate, due to the h^3 term in Eq. (10). The flow passage height variation across the fluid chamber is less than 1.5 μm , with a measured variation less than 1.1 μm ($\pm 0.55 \mu\text{m}$) for $h=40 \mu\text{m}$, which is 2.75% of h . The value 2.75% is the maximum percent variation of flow passage height for all flow passage heights tested. The resulting uncertainty magnitudes associated with experimentally measured pressure rise, flow passage height, fluid viscosity, disk rotational speed, pump chamber radii, and flow rate are presented in Table 2.

Results and Discussion

The experimental results are presented in five sections. The first section discusses pressure rise and flow rate variations for the single-disk viscous pump (single-DVP) with a flow passage height of 117 μm . The second section presents data showing the effects of changes in rotational speed on the pressure rise and flow rate of the single-DVP. The third section gives data showing the effects of changes in flow passage height on the flow rate and pressure

Table 2 Uncertainties associated with experimental data

Variable	Maximum percent uncertainty
ΔP_{2-1} (experimental)	5%
Q	2.5%
h	2.75%
μ	2%
ω	1.5%
R_1, R_2	1.1%

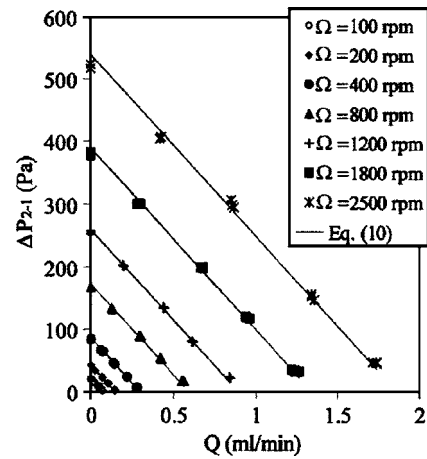


Fig. 6 Variations of pressure rise with flow rate for the single-disk viscous pump with a flow passage height of $h=117 \mu\text{m}$. Working fluid is water.

rise characteristics. The fourth section presents data which illustrate the effects of changes in fluid viscosity on the flow rate and pressure rise. The fifth section discusses performance of the single-DVP relative to a variety of other types of microscale pumps.

Pressure Rise and Flow Rate Variations. The dependence of pressure rise on flow rate for a flow passage height of 117 μm is illustrated by the data given in Fig. 6. These experimental data are obtained using water as the working fluid, with rotational speeds (Ω) between 100 and 2500 rpm. For a constant rotational speed, the flow rate is varied by changing the adjustable valve shown in Fig. 5. The solid lines in Fig. 6 represent theoretical values determined using Eq. (10). The data in Fig. 6 show that there is a linear relationship between the pressure rise and flow rate for the single-DVP for each different impeller rotational speed, which is consistent with results from a variety of macroscale viscous pumps [28–34]. This figure also shows that experimental data are in agreement with Eq. (10). The slopes of the data for each rotational speed in Fig. 6 are approximately the same, which means that ΔP_{2-1} versus Q slope is independent of rotational speed. The slopes of these data are characterized by the maximum pressure rise for $Q=0$, and the maximum flow rate at $\Delta P_{2-1}=0$. Similar trends of pressure rise and flow rate are observed for flow passage heights of 40, 73, and 246 μm . The data given in Fig. 6 also show that the single-DVP with a flow passage height of 117 μm is useful for applications that require pressure rises from 22 to 525 Pa and flow rates up to 1.75 ml/min.

Effects of Rotational Speed. The flow rate and pressure rise are varied to meet application requirements by changing the rotational speed. The data presented previously in Fig. 6 show that the slopes of the pressure rise and flow rate characteristics of the single-DVP are characterized by the maximum pressure rise and maximum flow rate. Therefore, the maximum pressure rise variations with rotational speed for $Q=0$, and the maximum flow rate variations with rotational speed for $\Delta P_{2-1}=0$ are presented.

When the flow rate is set to zero, Eq. (10) shows that the pump pressure rise varies linearly with rotational speed. Figure 7 shows such data for flow passage heights of 40, 73, 117, and 246 μm . The working fluid is water, and the rotational speed ranges between 100 and 3200 rpm for each constant flow passage height. Included is a theoretical line for each flow passage height determined from Eq. (10). The pressure rise increases linearly with rotational speed for each flow passage height in Fig. 7 and represents the maximum pressure rise between the pressure ports in the

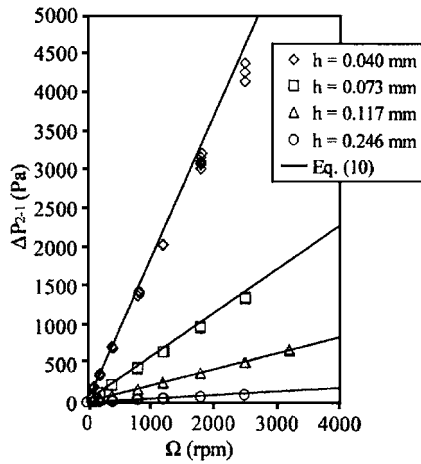


Fig. 7 Variations of pressure rise with rotational speed for the single-disk viscous pump. Working fluid is water, and $Q=0$.

single-DVP. Note that this maximum pressure is not the maximum pressure between the inlet and outlet ports, because the pressure continues to increase as it approaches the fluid outlet port.

Magnitudes of the viscous pump maximum pressure rise between the inlet and outlet ports (ΔP_{out-in}) are given in Fig. 8 for zero net flow rate and a flow passage height of 73 μm . Also included is the pressure rise between the pressure ports (ΔP_{2-1}). The experimental pressure rise data between the inlet and outlet ports are obtained by connecting the inlet and outlet tubing to the ports of a differential pressure transducer, which results in a zero net flow rate in the pump. This zero net flow condition is used because this arrangement gives the maximum pressure rise. The theoretical line for the pressure rise ΔP_{out-in} is obtained using $\Delta\theta=1.067\pi$ in Eq. (10) instead of $\Delta\theta=\pi/2$, where $\Delta\theta=1.067\pi$ corresponds to the angular span of the shear channel between the edges of the fluid inlet and outlet ports. Figure 8 shows that Eq. (10) gives a good representation of both ΔP_{out-in} and ΔP_{2-1} . Thus, the pressure rise between the inlet and outlet ports is approximately 2.13 times greater than the measured pressure rise between the pressure ports for this pump chamber geometry, for any given flow rate, rotational speed, or flow passage height.

Variations of maximum flow rate with rotational speed are shown in Fig. 9 for flow passage heights of 40, 73, 117, and

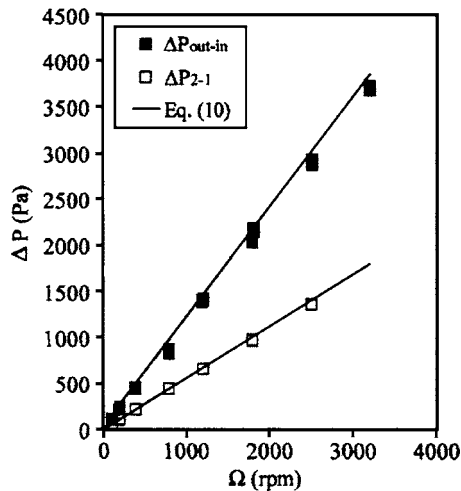


Fig. 8 Variations of pressure rise with rotational speed for the single-disk viscous pump with a flow passage height of $h = 73 \mu\text{m}$. Working fluid is water, and $Q=0$.

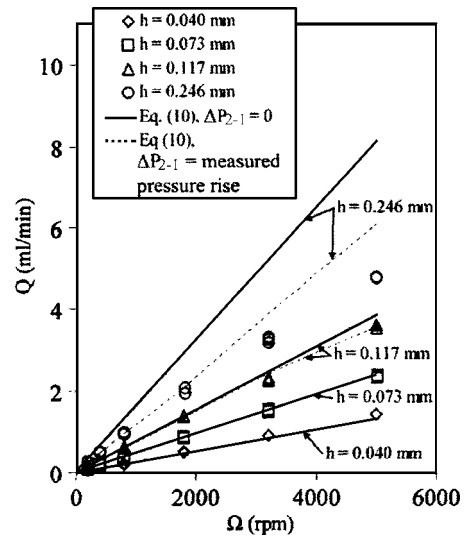


Fig. 9 Variations of maximum flow rate with rotational speed for the single-disk viscous pump. Working fluid is water.

246 μm . These data are obtained with a fully open adjustable valve in Fig. 5. The solid lines in Fig. 9 represent theoretical values determined by setting the pressure rise $\Delta P=0$ in Eq. (10). For flow passage heights of 117 and 246 μm , experimental flow rates deviate more significantly from theoretical flow rates as the rotational speed increases. This more significant deviation is due to additional experimental fluid losses through the inlet and outlet tubing. Such losses are present for all flow passage heights tested, but the effects are negligible for flow passage heights less than about 100 μm . Better agreement between theory and experimental data in Fig. 9 is obtained when losses in the inlet and outlet tubing, represented by the experimentally measured pressure rise (ΔP_{2-1}), are included in the analysis, and is shown by the dashed lines in Fig. 9. Note that the Reynolds number for the single-DVP with a flow passage height of 246 μm is 229.3 for a rotational speed of 5000 rpm, where Reynolds number is defined as

$$\text{Re} = \frac{\rho\omega(R_2 + R_1)h}{2\mu} \quad (11)$$

One assumption made in deriving Eq. (10), is that the Reynolds number is small. The data in Fig. 9 suggest that Eq. (10) is valid for $\text{Re} < 110$ for a flow passage height of 246 μm , which corresponds to a rotational speed of 2400 rpm. This range of Reynolds number validity is a result of neglecting advection terms in Navier-Stokes Eq. (1). However, note that some of these advection terms are considered to be negligible because the flow in the passage is maintained at or near to a fully developed condition.

Effect of Flow Passage Height. To meet application requirements, the flow rate and pressure rise are varied by changing the flow passage height. The data presented previously in Fig. 6 show that the slopes of the pressure rise and flow rate characteristics of the single-DVP are characterized by the maximum pressure rise and maximum flow rate. Therefore, the maximum pressure rise variations with rotational speed for $Q=0$, and the maximum flow rate variations with rotational speed for $\Delta P_{2-1}=0$ are presented.

Variations of pressure rise with flow passage height, for different disk rotational speeds, are shown in Fig. 10. These experimental data are obtained with a net zero flow rate in order to show the maximum pressure rise for each flow arrangement. The solid lines represent the pressure rise determined from Eq. (10), for the different flow passage heights and rotational speeds, and are in good agreement with experimental data. Note the increase in pressure rise as the flow passage height decreases for a particular disk

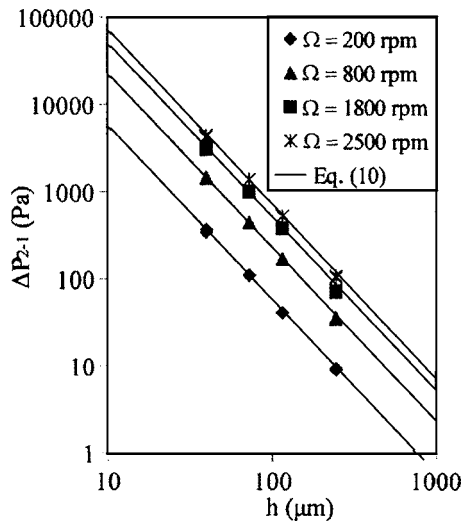


Fig. 10 Variations of maximum pressure rise with flow passage height for the single-disk viscous pump. Working fluid is water, and $Q=0$.

rotational speed. For $Q=0$, this pressure rise scales with flow passage height according to the relation given by

$$\Delta P_{2-1}(Q=0) \propto \frac{1}{h^2} \quad (12)$$

which is consistent with Eq. (10).

Variations of maximum flow rate with flow passage height are shown in Fig. 11 for rotational speeds (Ω) between 200 to 5000 rpm. Note that the flow rate decreases as flow passage height decreases for each rotational speed. The solid lines represent flow rate determined using Eq. (10) with the pressure rise set to zero. The dashed lines represent the flow rates determined using Eq. (10) including experimentally measured pressure rise contributions. The experimentally measured pressure rise is due to fluid losses through the inlet and outlet tubing. Note that the pressure rises due to these fluid losses are insignificant for flow passage heights less than or equal to about 100 μm . For the zero pressure rise condition shown in Fig. 11, flow rates scale with flow passage height according to the equation that has the form

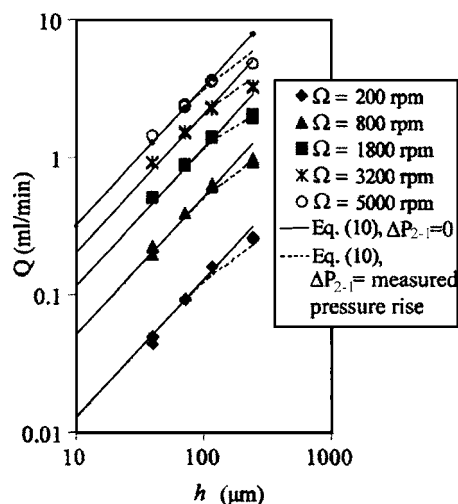


Fig. 11 Variations of maximum flow rate with flow passage height for the single-disk viscous pump. Working fluid is water.

Table 3 Shear rates for different pump chamber heights, and disk rotational speeds

h (μm)	Ω (rpm)	$\gamma_{\text{max}}(Q=0)$ (s^{-1})	$\gamma_{\text{average}}(Q=0)$ (s^{-1})	$\gamma_{\text{max}}(\Delta P=0)$ (s^{-1})	$\gamma_{\text{average}}(\Delta P=0)$ (s^{-1})
40	500	8.5×10^3	4.0×10^3	3.1×10^3	2.3×10^2
73	500	4.7×10^3	2.2×10^3	1.7×10^3	1.3×10^2
117	500	2.9×10^3	1.4×10^3	1.1×10^3	8.0×10^2
246	500	1.4×10^3	6.4×10^2	5.1×10^2	3.8×10^2
40	5000	8.5×10^4	4.0×10^4	3.1×10^4	2.3×10^4
73	5000	4.7×10^4	2.2×10^4	1.7×10^4	1.3×10^4
117	5000	2.9×10^4	1.4×10^4	1.1×10^4	8.0×10^3
246	5000	1.4×10^4	6.4×10^3	5.1×10^3	3.8×10^3

$$Q(\Delta P_{2-1}=0) \propto \frac{1}{h} \quad (13)$$

which is consistent with flow rate scaling in Couette flow between parallel plates with one translating plate [37].

Table 3 gives the maximum and average shear rates in the pump chamber for different pump chamber heights and rotational speeds. The maximum shear rate occurs on the surface of the rotating disk. The maximum and average shear rates increase linearly with rotational speed. The maximum shear rate increases as the pressure rise increases. The lowest value is present for the flow condition when $\Delta P=0$, and the highest value is present for the flow condition when $Q=0$. All shear rate values in Table 3 are below 10^5 1/s, which is the lowest shear rate that causes hemolysis of red blood cells.

Effects of Fluid Viscosity. Figure 12 shows the experimentally measured variations of flow rates and rotational speed for the single-DVP with water and oil as the working fluids, and a flow passage height of 117 μm . The solid line represents flow rates obtained using Eq. (10). The fluid properties for water and oil are given in Table 1. Note that the variation of dimensional volumetric flow rate with rotational speed is linear and independent of fluid viscosity. Figure 13 shows corresponding pressure rise data. Here, pressure rises increase linearly with rotational speed, such that values with oil as the working fluid are about two orders of magnitude larger than the values obtained with water as the working fluid.

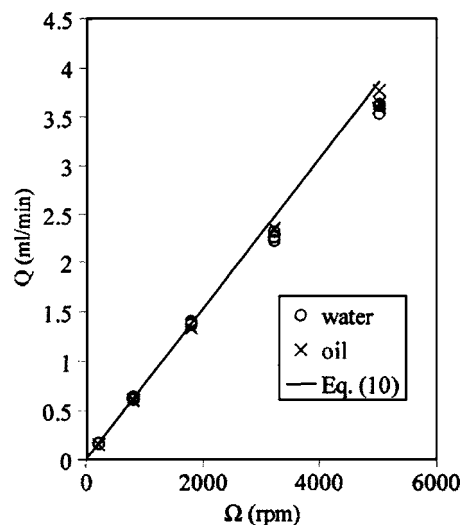


Fig. 12 Variations of maximum flow rate with rotational speed variation for the single-disk viscous pump with a flow passage height of 117 μm . Working fluid is water or 5W-30 oil.

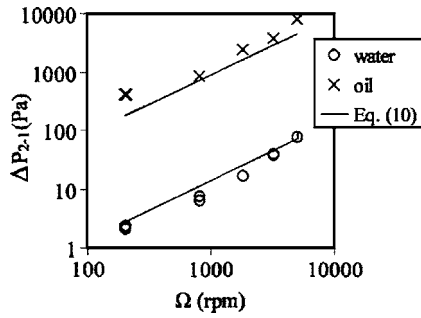


Fig. 13 Variations of pressure rise with rotational speed for the single-disk viscous pump data shown in Fig. 12. The flow passage height is $117 \mu\text{m}$, and the working fluid is water or 5W-30 oil.

Performance of the Single-Disk Pump Relative to Other Microscale Pumps. The maximum flow rate of the single-DVP and several different micropumps are shown in Fig. 14. The typical size of the micropumps is defined as the membrane diameter, disk diameter, or channel width. The size of the actuator is not included when determining the typical size. The data points for the single-DVP are the maximum flow rate for a flow passage height of 40 and $246 \mu\text{m}$, at a rotational speed of 2500 rpm, with water or oil as the working fluid. The viscous pump data point furthest to the right is the maximum flow rate presented by Sen [15], and the other viscous pump data point is the maximum experimental flow rate data presented by Kilani [14]. The single-DVP produces higher flow rates than many other reported micropumps of similar size.

Figure 15 shows the variations of pressure rise and flow rate of the single-DVP and several other micropumps with typical sizes less than 15 mm. The single-DVP produces higher pressure rises than many other reported micropumps for similar flow rates. The data in Fig. 15 also show that single-DVP is good for a wide range of flow rates, and pressure rises.

Summary and Conclusions

A pump called the single-disk viscous pump (single-DVP) is developed and tested. The single-DVP consists of a 10.16 mm diameter disk that rotates above a C-shaped channel with inner

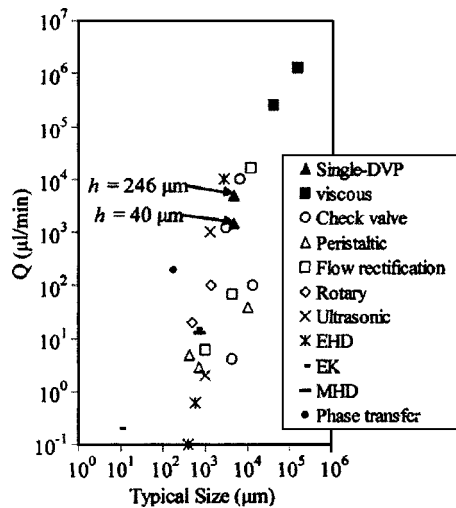


Fig. 14 Volumetric flow rate and typical size for various micropumps. Typical size is defined as the membrane diameter, disk diameter, or channel width. The data points for the single-DVP are for flow passage heights of $h=40$, and $h=246$, at a rotational speed 2500 rpm [2–26].

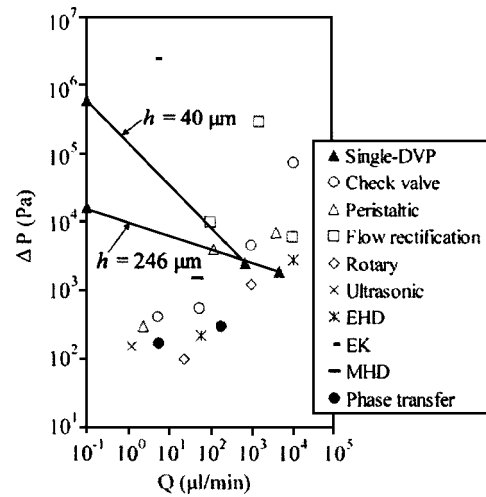


Fig. 15 Pressure rise and flow rate for various micropumps. For all points other than the single-DVP, the data corresponds to the maximum flow rate and maximum pressure. The data shown for the single-DVP are for 5W-30 motor oil at a rotational speed of 2500 rpm [2–9,11,13,16–19,22–25].

and outer radii of 1.19 and 2.38 mm, respectively, and a channel depth of 40 , 73 , 117 , or $246 \mu\text{m}$. Fluid inlet and outlet ports are located at the ends of the C-shaped channel. The advantages of this micropump compared to other micropumps and viscous pumps include analytic tractability, a wide range of possible flow rates, simplicity, constant flow, flow rate independent of fluid viscosity, planar structure, well controlled flow rate, and the ability to pump delicate fluids without disruption or damage. The design of the disk pumps is simple, and can potentially be fabricated using microfabrication technology due to the planar structure of the pump, or using injection molding techniques. The pump chamber is symmetric and the flow direction can be reversed by changing the disk rotational direction. The experimental flow rates and pressure rises are well represented by Eq. (10) for rotational speeds of 100 – 5000 rpm, fluid viscosities of 1 – 62 mPa s, flow passage heights of 40 – $246 \mu\text{m}$, pressure rises of 0 – 31.1 kPa, and flow rates of 0 – 4.75 ml/min. The deviation between Eq. (10) and experimental data increases for Reynolds numbers greater than 110 .

The experimental and theoretical pressure rises show a nearly linear relationship for variation in flow rate. The pressure rise variations with flow rate for the single-DVP are characterized by a straight line between the maximum pressure rise (at zero net flow) and maximum flow rate (at zero pressure rise). For $Q=0$, the pressure rise varies linearly with rotational speed. The pressure rise also increases as the flow passage height decreases for a particular rotational speed. For $\Delta P=0$, the maximum volumetric flow rate is achieved, and is found to vary linearly with rotational speed. The volumetric flow rate of the single-DVP is independent of fluid viscosity for a given fluid circuit. The pressure rise through the pump chamber can be increased by increasing the rotational speed, increasing the fluid viscosity, increasing the circumferential span of the shear channel, or by decreasing the flow passage height. The flow rate through the pump chamber can be increased by increasing the flow passage height, increasing the rotational speed, or increasing the width of the pumping chamber.

The efficiency of the single-disk viscous pump can be determined using $\eta = \Delta P Q / T \omega$. A typical efficiency of the present device for a rotational speed of 1000 rpm, pump chamber height of $117 \mu\text{m}$, and water as the working fluid is estimated to be approximately 0.25 or 25% . As such, this value does not account for any type of motor losses.

Acknowledgment

Work presented in this paper was supported by the National Science Foundation (NSF) through the IGERT Program, Grant Number DGE 9987616.

Nomenclature

- h = flow passage height of the disk pump
 p = static pressure
 p_1 = static pressure at pressure port 1
 p_2 = static pressure port 2
 ΔP = static pressure rise
 ΔP_{2-1} = static pressure rise between pressure ports = $(p_2 - p_1)$
 ΔP_{out-in} = static pressure rise between the fluid inlet and outlet ports
 Q = volumetric flow rate
 r = radial location
 R_1 = inner radius of the pump chamber
 R_2 = outer radius of the pump chamber
 Re = Reynolds number
 T = pump torque
 v = fluid velocity
 v_r = radial fluid velocity
 v_z = fluid velocity in the z direction
 v_θ = fluid velocity in the θ direction
 z = direction normal to disk surface

Greek Symbols

- μ = dynamic viscosity
 ρ = fluid density
 η = pump efficiency
 $\gamma_{average}$ = average shear rate in pump chamber, $\gamma_{average} = [1/h(R_2 - R_1)] \int_0^h \int_{R_1}^{R_2} \partial v_\theta / \partial z dr dz$
 γ_{max} = maximum shear rate in pump chamber, generally located on the surface of the rotating disk
 ω = rotational speed of the disk (rad/s)
 Ω = rotational speed of the disk (rpm)
 θ = angle
 $\Delta\theta$ = angular span between two locations

References

- [1] Nhuyen, N.-T., and Wereley, S. T., 2002, *Fundamentals and Applications of Microfluidics*, Artech House, Inc., Norwood, pp. 292–337.
[2] Olsson, A., Steeme, G., and Steeme, E., 1995, "A Valve-less Planar Fluid Pump With Two Pump Chambers," *Sens. Actuators, A*, **47**(2), pp. 549–556.
[3] Tsia, J. H., and Lin, L., 2002, "A Thermal Bubble Actuated Micro Nozzle-Diffuser Pump," *J. Microelectromech. Syst.*, **11**(6), pp. 665–668.
[4] Nguyen, N. T., and Huang, X. Y., 2001, "Miniature Valveless Pumps Based on Printed Circuit Board Technique," *Sens. Actuators, A*, **88**(2), pp. 104–111.
[5] Benard, W. L., Kahn, H., Heuer, A. H., and Huff, M. S., 1998, "Thin Film Shape-Memory Alloy Actuated Micropumps," *J. Microelectromech. Syst.*, **7**(2), pp. 245–251.
[6] Meng, E., Wang, X.-Q., Jak, H., and Tai, Y.-C., 2000, "A Check-Valved Silicone Diaphragm Pump," *Proceedings of MEMS '00*, 13th International Workshop Micro ElectroMechanical Systems, Japan, Jan 23–27, pp. 23–27.
[7] Gass, V., Van der Schoot, G. H., Jeanneret, S., and DeRooij, N. F., 1994, "Integrated Flow-Regulated Silicon Micropump," *Sens. Actuators, A*, **43**, pp. 335–338.
[8] Saggere, L., Hagood, N. W., Roberts, D. C., Li, H. Q., Steyn, J. L., Turner, K., Carretero, J. A., Yaglioglu, O., Su, Y. H., Mlcak, R., Spearing, S. M., Breuer, K. S., and Schmidt, M. A., 2000, "Design, Fabrication, and Testing of a Piezoelectrically Driven High Flow Rate Micro-pump," *Proceedings of the 12th IEEE International Symposium on Applications of Ferroelectrics*, Vol. 1, July–Aug, pp. 297–300.
[9] Richter, A., Plettner, A., Hofmann, K. A., and Sandmaier, H., 1991, "A Micromachined Electrohydrodynamic (EHD) Pump," *Sens. Actuators, A*, **29**, pp.

- 159–168.
[10] Fuhr, G., Hagedorn, R., Muller, T., Benecke, W., and Wagner, B., 1992, "Microfabricated Electrohydrodynamic (EHD) Pumps for Liquids of Higher Conductivity," *J. Microelectromech. Syst.*, **1**(3), pp. 141–146.
[11] Ahn, S. H., and Kim, Y. K., 1998, "Fabrication and Experiment of a Planar Micro Ion Drag Pump," *Sens. Actuators, A*, **70**, pp. 1–5.
[12] Furuya, A., Shimokawa, F., Matsuura, T., and Sawada, R., 1996, "Fabrication of Fluorinated Polyimide Microgrids Using Magnetically Controlled Reactive Ion Etching (MC-RIE) and Their Applications to a Ion Drag Integrated Micropump," *J. Micromech. Microeng.*, **6**, pp. 310–319.
[13] Zeng, S., Chen, C. H., Mikkelsen, J. C., and Santiago, J. G., 2000, "Fabrication and Characterization of Electrokinetic Micro Pumps," 7th Intersociety Conference on Thermal and Thermomechanical Phenomena in Electronic Systems, CPMT/IEEE, Las Vegas, Vol. 2, pp. 31–36.
[14] Kilani, M., Galambos, P., Haik, Y., and Chen, C. J., 2003, "Design and Analysis of a Surface Micromachined Spiral-Channel Viscous Pump," *J. Fluids Eng.*, **125**(2), pp. 339–344.
[15] Sen, M., Wajerski, D., and Gad-El-Hak, M., 1996, "A Novel Pump for MEMS Applications," *J. Fluids Eng.*, **118**(3), pp. 624–627.
[16] Ahn, C. H., and Allen, M. G., 1995, "Fluid Micropumps Based on Rotary Magnetic Actuators," *Proceedings of MEMS 1995*, Jan.–Feb., pp. 408–418.
[17] Dopfer, J., Clemens, M., Ehrfeld, W., Jung, S., Kamper, K.-P., and Lehr, H., 1997, "Micro Gear Pumps for Dosing of Viscous Fluids," *J. Micromech. Microeng.*, **7**(2), pp. 230–232.
[18] Mizoguchi, H., Ando, M., Mizuno, T., Takagi, T., and Nakajima, N., 1992, "Design and Fabrication of Light Driven Micropump," *Proceedings of MEMS '92*, 5th IEEE Int. Workshop MEMS, Germany, Jan. 25–28, pp. 31–36.
[19] Grosjean, C., and Tai, Y. C., 1999, "A Thermopneumatic Peristaltic Micropump," *Proceedings of Transducer '99*, the 10th Int. Conf. on Solid State Sensors and Actuators, Japan, June 7–10, pp. 1776–1779.
[20] Cabuz, C., Herb, W. R., Cabuz, E. I., and Lu, S. T., 2001, "The Dual Diaphragm Pump," *Proceedings of MEMS '01*, 14th IEEE Int. Workshop MEMS, Switzerland, Jan. 21–25, pp. 519–522.
[21] Luginbuhl, Ph., Collins, S. D., Racine, G. A., Grettillat, M. A., de Rooij, N. F., Brooks, K. G., and Setter, N., 1997, "Flexural-Plate-Wave Actuators Based on PZT Thin Films," *Proceedings of MEMS '97*, Jan, 1997, pp. 327–332.
[22] Miyazaki, S., Kawai, T., and Araragi, M., 1991, "A Piezoelectric Pump Driven by a Flexural Progressive Wave," *Proceedings of MEMS '91*, 4th International Workshop MEMS, Japan, Jan. 30–Feb. 4, pp. 283–288.
[23] Takagi, H., Maeda, R., Ozaki, K., Parameswaran, M., and Mehta, M., 1994, "Phase Transformation Type Micropump," *Proceedings of International Symposium on Micro Machine and Human Systems*, Japan, Oct., pp. 199–202.
[24] Geng, X., Yuan, H., Oguz, H. N., and Prosperetti, A., 2001, "Bubble-Based Micropump for Electrically Conducting Liquids," *J. Micromech. Microeng.*, **11**, pp. 270–276.
[25] Hatch, A., Kamholz, A. E., Holman, G., Yager, P., and Bohringer, K. F., 2001, "A Ferrofluidic Magnetic Micropump," *J. Microelectromech. Syst.*, **10**(2), pp. 215–221.
[26] Huang, L., Wang, W., Murphy, M. C., Lian, K., and Ling, Z. G., 2000, "LIGA Fabrication and Test of a DDC Type Magnetohydrodynamic (MHD) Micropump," *Microsyst. Technol.*, **6**, pp. 235–240.
[27] Karniadakis, G. E., and Beskok, A., 2002, *Micro Flows, Fundamentals and Simulation*, Springer, New York, pp. 1–31.
[28] Etsion, I., and Yaier, A., 1988, "Performance Analysis of a New Concept Viscous Pump," *J. Tribol.*, **110**, pp. 93–99.
[29] Winoto, S. H., and Yohanand, K., 1994, "Analysis and Test of a Viscous Pump With Radial Pumping Grooves," *Tribol. Trans.*, **37**(4), pp. 691–700.
[30] Arafa, H. A., and Osman, T. A., 2003, "Hydrostatic Bearings With Multiport Viscous Pumps," *Proc. Inst. Mech. Eng., Part J: J. Eng. Tribol.*, **217**, pp. 333–342.
[31] Sato, Y., and Knight, J. D., 1992, "Performance Characteristics of Shrouded Rayleigh-step and Spiral Groove Viscous Pumps," *J. Tribol.*, **114**, pp. 499–506.
[32] Elrod, H. G., 1973, "Some Refinements of the Theory of the Viscous Screw Pump," *J. Lubr. Technol.*, **95**(1), pp. 82–93.
[33] Mainland, M., and Green, I., 1992, "Analysis and Optimization of Semicircular and Straight Lobe Viscous Pumps," *J. Tribol.*, **114**(3), pp. 515–523.
[34] Hasinger, S. H., and Kehrt, L. G., 1963, "Investigation of a Shear-Force Pump," *J. Eng. Power*, **85**, pp. 201–207.
[35] Sharatchandra, M. C., Sen, M., and Gad-el-Hak, M., 1997, "Navier-Stokes Simulations of a Novel Viscous Pump," *J. Fluids Eng.*, **119**, pp. 372–382.
[36] Blanchard, D., Ligrani, P., and Gale, B., 2004, "Rotary Centrifugal and Viscous Micropumps," US Patent Office, Application No. PCT/US2004/028890, September 3.
[37] Panton, R. L., 1996, *Incompressible Flow*, 2nd ed., New York, New York, pp. 148–154, 158–160, 660–664.
[38] Moffat, R. J., 1982, "Contributions to the Theory of Single-Sample Uncertainty Analysis," *J. Fluids Eng.*, **104**, pp. 250–260.